24th Applied Aerodynamics Conference
5 - 8 June 2006, San Francisco, California

AIAA 2006-3455

OPTIMUM SHAPE DESIGN FOR UNSTEADY THREE- DIMENSIONAL VISCOUS FLOWS USING A NON- LINEAR FREQUENCY DOMAIN METHOD

Siva K. Nadarajah *
Department of Mechanical Engineering
McGill University
Montreal, QC H3A 2S6 Canada

Antony Jameson †
Department of Aeronautics and Astronautics
Stanford University
Stanford, California 94305 U.S.A.

This paper presents an adjoint method for the optimum shape design of unsteady three-dimensional viscous flows. The goal is to develop a set of discrete unsteady adjoint equations and the corresponding boundary condition for the non-linear frequency domain method. First, this paper presents the complete formulation of the time dependent optimal design problem. Second, we present the non-linear frequency domain adjoint equations for three-dimensional viscous transonic flows. Third, we present results that demonstrate the application of the theory to a three-dimensional wing.

I. Introduction

There are numerous important engineering applications in which the flow is inherently unsteady but periodic. Helicopter rotors in forward flight, turbomachinery blades and cooling fans operate in unsteady flow and are constantly subjected to unsteady loads. Optimization techniques for unsteady flows are clearly needed to improve their performance, and to alleviate the unsteady effects that contribute to flutter, buffeting, poor gust and acoustic response, and dynamic stall. As yet there have been few efforts in this direction.

One of the major reasons is the demanding computational cost associated with the calculation of unsteady flows. As part of the Accelerated Strategic Computing Initiative (ASCI) project at Stanford, Davis[2] presented estimates for the computational cost of a multistage compressor and turbine calculation based on the parallel execution of 750 processors operating 8 hours a day. He concluded that it would require 1300 days to compute the flow through a 23 blade row compressor. The overwhelming majority of the computational time is spent on time accurately resolving the decay of the initial transients. Although this example is an extreme case, it illustrates the prohibitive cost of many unsteady calculations using time accurate solvers to find a periodic steady state.

Nevertheless, the development of optimum shape design for two-dimensional unsteady flows using the time accurate adjoint based design approach has been pursued by Nadarajah and Jameson.[14,17] This work is largely based on algorithms developed for Aerodynamic Shape Optimization (ASO) for a steady flow environment.[6,8,15,18,19] Nadarajah derived and applied the time accurate adjoint equations (both the continuous and discrete) to the redesign of an oscillating airfoil in an inviscid transonic flow. The redesigned shape achieved a reduction in the time-averaged drag while maintaining the time-averaged lift. The approach

---

[*] Assistant Professor, Member AIAA

[†] Thomas V. Jones Professor of Engineering, Stanford University, AIAA Fellow

utilized a dual time stepping[7] technique that implements a fully implicit second order backward difference formula to discretize the time derivative. Typical runs required 15 periods with 24 discrete time steps per period, and 15 multigrid cycles at each time step. Encouraging results were obtained at a substantial computational expense.

The prohibitive cost of computing three dimensional unsteady flows using the time accurate approach has motivated a new interest in using periodic methods. Linearized frequency domain and deterministic-stress[1] methods are examples of periodic methods. However, these methods generally do not account for strong nonlinearities in the system. Pseudo spectral approaches in space and time have been implemented for a multitude of non-linear problems throughout the numerical analysis literature. The Harmonic Balance technique proposed by Hall et al.[4,5] represents the first pseudo-spectral method in time for the unsteady Euler equations. The Non-Linear Frequency Domain method (NLFD) proposed by McMullen et al.[10,11] is a similar approach that was later validated for the unsteady Navier-Stokes equations. These approaches are spectral techniques which converge at an exponential rate to the exact solution, even in the presence of aliasing affects.[20] This can be compared to more classical finite difference schemes which contain error proportional to some power of the grid spacing. An analysis presented in McMullen's thesis[12] demonstrates the comparative advantage of spectral techniques for real world applications. Using an unsteady pitching airfoil in a transonic flow, he calculated the error in the magnitude of the fundamental harmonic for the coefficient of lift. The data showed that an NLFD calculation employing one time varying harmonic (which can be represented with three discrete samples) produced an error level equivalent to that of a time accurate calculation using 45 time steps per period. For this case, the NLFD calculation was roughly an order of magnitude more efficient than time accurate codes operating at equivalent error levels.

Recently, there have been two investigations into the modeling of unsteady aerodynamic design sensitivities. Duta et. al.[3] have presented a harmonic adjoint approach for unsteady turbomachinery design. The aim of the work was to reduce blade vibrations due to flow unsteadiness. The research produced adjoint methods that were based on a linearized analysis of periodic unsteady flows. Thomas et al.[21] presented a viscous discrete adjoint approach for computing unsteady aerodynamic design sensitivities. The adjoint code was generated from the harmonic balance flow solver with the use of an automatic differentiation software compiler.

The work presented in this paper is a viscous extension of an inviscid study presented at the 44th Aerospace Sciences Meeting and Exhibit, January 9–12, 2006 in Reno, Nevada.[16] The motivation of the research has been fueled both by the success of our current capability for automatic shape optimization for unsteady flows and the future potential of the NLFD method. The result of this effort is a NLFD adjoint design code that is fully non-linear and the computational cost of the adjoint module is proportional to the cost of the flow solver.

II. Governing Equations

The Cartesian coordinates and velocity components are denoted by x_1, x_2, x_3, and u_1, u_2, and u_3. Einstein notation simplifies the presentation of the equations, where summation over $k = 1$ to 3 is implied by a repeated index k. The three-dimensional Navier-Stokes equations then take the form,

$$\frac{\partial w}{\partial t} + \frac{\partial f_i}{\partial x_i} = \frac{\partial f_{vi}}{\partial x_i} \quad \text{in } \mathcal{D}, \tag{1}$$

where the state vector w, inviscid flux vector f and viscous flux vector f_v are described respectively by

$$w = \left\{ \begin{array}{c} \rho \\ \rho u_1 \\ \rho u_2 \\ \rho u_3 \\ \rho E \end{array} \right\}, \quad f_i = \left\{ \begin{array}{c} \rho(u_i - b_i) \\ \rho u_1(u_i - b_i) + p\delta_{i1} \\ \rho u_2(u_i - b_i) + p\delta_{i2} \\ \rho u_3(u_i - b_i) + p\delta_{i3} \\ \rho E(u_i - b_i) + p u_i \end{array} \right\}, \quad \text{and} \quad f_{vi} = \left\{ \begin{array}{c} 0 \\ \sigma_{ij}\delta_{j1} \\ \sigma_{ij}\delta_{j2} \\ \sigma_{ij}\delta_{j3} \\ u_j\sigma_{ij} + k\frac{\partial T}{\partial x_i} \end{array} \right\}. \tag{2}$$

In these definitions, ρ is the density, u_i, b_i are the Cartesian velocity components of the fluid and boundary respectively, E is the total energy and δ_{ij} is the Kronecker delta function. The pressure is determined by the equation of state

$$p = (\gamma - 1)\,\rho \left\{ E - \frac{1}{2}\left(u_i u_i\right) \right\},$$

and the stagnation enthalpy is given by

$$H = E + \frac{p}{\rho},$$

where γ is the ratio of the specific heats. The viscous stresses may be written as

$$\sigma_{ij} = \mu \left(\frac{\partial u_i}{\partial x_j} + \frac{\partial u_j}{\partial x_i} \right) + \lambda \delta_{ij} \frac{\partial u_k}{\partial x_k}, \tag{3}$$

where μ and λ are the first and second coefficients of viscosity. The coefficient of thermal conductivity and the temperature are computed as

$$k = \frac{c_p \mu}{Pr}, \qquad T = \frac{p}{R\rho}, \tag{4}$$

where Pr is the Prandtl number, c_p is the specific heat at constant pressure, and R is the gas constant.

For discussion of real applications using a discretization on a body conforming structured mesh, it is also useful to consider a transformation to the computational coordinates (ξ_1,ξ_2,ξ_3) defined by the metrics

$$K_{ij} = \left[\frac{\partial x_i}{\partial \xi_j} \right], \quad J = \det\left(K\right), \quad K_{ij}^{-1} = \left[\frac{\partial \xi_i}{\partial x_j} \right].$$

The simulations contained in this research are restricted to rigid mesh translation. As a result, we can write equation (1) as the product of the cell volume and temporal derivative of the state vector w at the cell center. In terms of cell volumes and the local residual $R(w)$ (comprised of both convective and dissipative fluxes), equation (1) can be written in semi-discrete form as

$$V \frac{\partial w}{\partial t} + R(w) = 0 \quad \text{in } \mathcal{D}, \tag{5}$$

where, the residual $R(w)$ can then be written in computational space as

$$R(w) = \frac{\partial \left(F_i - F_{vi}\right)}{\partial \xi_i}, \tag{6}$$

where the inviscid and viscous flux contributions are now defined with respect to the computational cell faces by $F_i = S_{ij} f_j$ and $F_{vi} = S_{ij} f_{vj}$, and the quantity $S_{ij} = J K_{ij}^{-1}$ represents the projection of the ξ_i cell face along the x_j axis. In obtaining equation (6) we have made use of the property that

$$\frac{\partial S_{ij}}{\partial \xi_i} = 0, \tag{7}$$

which represents the fact that the sum of the face areas over a closed volume is zero, as can be readily verified by a direct examination of the metric terms.

When equation (6) is formulated for each computational cell, a system of first-order ordinary differential equations is obtained. To eliminate odd-even decoupling of the solution and overshoots before and after shock waves, the conservative and viscous fluxes are added to a diffusion flux. The artificial dissipation scheme used in this research is a blended first and third order flux, first introduced by Jameson, Schmidt, and Turkel.[?] The blended first and third order artificial dissipation term is discretized as

$$d_{i+\frac{1}{2},j,k} = \nu^{(2)}_{i+\frac{1}{2},j,k} \Lambda_{i+\frac{1}{2},j,k} \Delta_{i+\frac{1}{2},j,k} - \nu^{(4)}_{i+\frac{1}{2},j,k} \Lambda_{i+\frac{1}{2},j,k} \left[\Delta_{i+\frac{3}{2},j,k} - 2\Delta_{i+\frac{1}{2},j,k} + \Delta_{i-\frac{1}{2},j,k} \right].$$

where $\Delta_{i+\frac{1}{2},j,k} = w_{i+1,j,k} - w_{i,j,k}$. The coefficients $\nu^{(2)}$ and $\nu^{(4)}$ are the products of the adjustable constants and the normalized second difference of the pressure. $\Lambda_{i+\frac{1}{2},j,k}$ is the rescaled numerical spectral radius of the flux Jacobian matrix and directionally scales the dissipative terms.

III. Formulation of the Time-Dependent Optimal Design Problem

Optimal control of time dependent trajectories is generally complicated by the need to solve the adjoint equation in reverse time from a final boundary condition using data from the trajectory solution, which in turn depends on the control derived from the adjoint solution.

Introduce the cost function

$$I = \int_0^{t_f} \mathcal{L}(w, f)dt + \mathcal{M}(w(t_f)),$$

where the function $\mathcal{L}$ depends on the flow solution w, and the shape function f and the function $\mathcal{M}$ depends on the time dependent flow solution. Assume that the following equation defines the time-dependent flow solution

$$V\frac{\partial w}{\partial t} + R(w, f) = 0,$$

where V is the cell volume and R represents a residue containing the convective and dissipative fluxes. A change in f results in a change

$$\delta I = \int_0^{t_f} \left(\frac{\partial \mathcal{L}^T}{\partial w}\delta w + \frac{\partial \mathcal{L}^T}{\partial f}\delta f\right) dt + \frac{\partial \mathcal{M}^T}{\partial w}\delta w(t_f),$$

in the cost function. The variation in the flow solution is

$$V\frac{\partial}{\partial t}\delta w + \frac{\partial R}{\partial w}\delta w + \frac{\partial R}{\partial f}\delta f = 0.$$

Next, introduce a Lagrange multiplier ψ to the time-dependent flow equation, integrate it over time and subtract it from the variation of the cost function to arrive at the following equation.

$$\begin{aligned}\delta I &= \int_0^{t_f} \left(\frac{\partial \mathcal{L}^T}{\partial w}\delta w + \frac{\partial \mathcal{L}^T}{\partial f}\delta f\right) dt + \frac{\partial \mathcal{M}^T}{\partial w}\delta w(t_f) \\ &- \int_0^{t_f} \psi^T \left(V\frac{\partial}{\partial t}\delta w + \frac{\partial R}{\partial w}\delta w + \frac{\partial R}{\partial f}\delta f\right) dt.\end{aligned}$$

By integrating the term $\int_0^{t_f} \psi^T V \frac{\partial}{\partial t}\delta w dt$ by parts, yields

$$\begin{aligned}\delta I &= \int_0^{t_f} \left(\frac{\partial \mathcal{L}^T}{\partial w} + V\frac{\partial \psi^T}{\partial t} - \psi^T\frac{\partial R}{\partial w}\right) \delta w dt \\ &+ \left(\frac{\partial \mathcal{M}^T}{\partial w} - \psi^T(t_f)\right) \delta w(t_f) \\ &+ \int_0^{t_f} \left(\frac{\partial \mathcal{L}^T}{\partial f} - \psi^T\frac{\partial R}{\partial f}\right) \delta f dt.\end{aligned}$$

Choose ψ to satisfy the adjoint equation

$$V\frac{\partial \psi}{\partial t} = \left(\frac{\partial R}{\partial w}\right)^T \psi - \left(\frac{\partial \mathcal{L}}{\partial w}\right)$$

with the terminal boundary condition

$$\psi(t_f) = \frac{\partial \mathcal{M}}{\partial w}.$$

Then

$$\delta I = \mathcal{G}^T \delta f,$$

where

$$\mathcal{G}^T = \int_0^{t_f} \left(\frac{\partial \mathcal{L}^T}{\partial f} - \psi^T\frac{\partial R}{\partial f}\right) dt.$$

The sensitivity derivatives are determined by the solution of the adjoint equation in reverse time from the terminal boundary condition and the time-dependent solution of the flow equation. These sensitivity derivatives are then used to get a direction of improvement and steps are taken until convergence is achieved.

The computational costs of unsteady optimization problems are directly proportional to the desired number of time steps. The unsteady flow calculation can be obtained either by the use of implicit time-stepping schemes or a NLFD approach.

IV. Development of the Non-Linear Frequency Domain Adjoint Equations

The derivation of the NLFD method starts with the semi-discrete form of the governing equations, and assumes that the solution w and spatial operator R can be represented by separate Fourier series:

$$\begin{aligned} w &= \sum_{k=-\frac{N}{2}}^{\frac{N}{2}-1} \hat{w}_k e^{ikt} \\ R &= \sum_{k=-\frac{N}{2}}^{\frac{N}{2}-1} \hat{R}_k e^{ikt} \end{aligned} \tag{8}$$

where,

$$i = \sqrt{-1}. \tag{9}$$

Here, however each coefficient $\hat{R}_k$ of the transform of the residual depends on all the coefficients $\hat{w}_k$, because $R(w(t))$ is a non-linear function of $w(t)$. Thus equation (10) represents a non-linear set of equations which must be iteratively solved. The solver attempts to find a solution, w, that drives this system of equations to zero for all wavenumbers, but at any iteration in the solution process the unsteady residual, R^*, will be finite:

$$\hat{R^*}_k = ikV\hat{w}_k + \hat{R}_k. \tag{10}$$

The nonlinearity of the unsteady residual stems from the spatial operator. There are two approaches to calculating the spatial operator expressed in the frequency domain. The first uses a complex series of convolution sums to calculate $\hat{R}_k$ directly from $\hat{w}_k$. This approach is discarded due to its massive complexity (considering artificial dissipation schemes and turbulence modeling) and cost that scales quadratically with the number of modes N. Instead, we implement a pseudo-spectral approach in time. This approach requires several transformations between the physical and frequency domains which are performed by a Fast Fourier Transform (FFT). The computational cost of this transform scales like $N\log(N)$, where N is a large number. A diagram detailing the transformations used by the pseudo spectral approach is provided in figure (1).

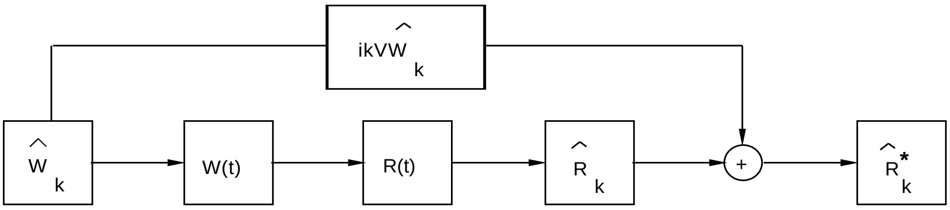

Figure 1. Simplified dataflow diagram of the time advancement scheme illustrating the pseudo spectral approach used in calculating the non-linear spatial operator R.

The pseudo-spectral approach begins by assuming that $\hat{w}_k$ is known for all wavenumbers. Using an inverse FFT, $\hat{w}_k$ can be transformed back to the physical space resulting in a state vector $w(t)$ sampled at evenly distributed intervals over the time period. At each of these time instances the steady-state operator $R(w(t))$ can be computed. A FFT is then used to transform the spatial operator to the frequency domain where $\hat{R}_k$ is known for all wavenumbers. The unsteady residual $\hat{R^*}_k$ can then be calculated by adding $\hat{R}_k$ to the spectral representation of the temporal derivative $ikV\hat{w}_k$.

Consistent with the time accurate approach, a pseudo-time derivative can be added, and a time-stepping scheme can be employed to numerically integrate the resulting equations.

$$V\frac{\partial \hat{w}_k}{\partial \tau} + \hat{R^*}_k = 0. \tag{11}$$

In the NLFD case, an unsteady residual exists for each wavenumber used in the solution and the pseudo-time derivative acts as a gradient to drive the absolute value of all of these components to zero simultaneously.

The NLFD discrete adjoint equation can be developed using two separate approaches. In the first approach, we first take a variation of the unsteady residual $\hat{R^*}_k$ represented in equation (10) with respect to the state vector $\hat{w}_k$ and shape function f, to produce

$$\delta\hat{R^*}_k = ikV\delta\hat{w}_k + \delta\hat{R}_k.$$

The next step, would be to expand $\delta\hat{R}_k$ as a function of $\hat{w}_k$. As mentioned earlier, this approach would require a series of convolution sums to express $\delta\hat{R}_k$ as a function of $\delta\hat{w}_k$. This method was not implemented due to its computational cost and added complexity. Instead, the adjoint equations were solved using a pseudo-spectral approach similar to the one applied to the flow equations.

In the latter approach, the NLFD adjoint equations are developed from the semi-discrete from of the adjoint equation, which can be as expressed as

$$V\frac{\partial \psi}{\partial t} + R(\psi) = 0,$$

where $R(\psi)$ is the sum of all the spatial operators, both convective and dissipative, used in the discretized adjoint equations. Refer to Nadarajah[17] for a detailed derivation of these spatial operators and boundary conditions. Next, we assume that the adjoint variable and spatial operator can be expressed as a Fourier series:

$$\begin{aligned} \psi &= \sum_{k=-\frac{N}{2}}^{\frac{N}{2}-1} \hat{\psi}_k e^{ikt}, \\ R(\psi) &= \sum_{k=-\frac{N}{2}}^{\frac{N}{2}-1} \widehat{R(\psi)}_k e^{ikt}. \end{aligned} \tag{12}$$

The derivation of the NLFD adjoint then follows that of the NLFD flow equations. The NLFD adjoint equations are expressed as

$$V\frac{\partial \hat{\psi}_k}{\partial \tau} + \widehat{R(\psi)}_k^* = 0.$$

where $\widehat{R(\psi)}_k^* = ikV\hat{\psi}_k + \widehat{R(\psi)}_k$. The pseudo-spectral approach illustrated in figure (1) is employed in the NLFD adjoint code to form the unsteady residual. This term in conjunction with a pseudo time derivative provides an iterative solution process consistent with that documented for the flow equations.

V. Design Process

The design process used in this work will change the shape of the wing in order to minimize its time-averaged coefficient of drag. Given the derivation provided in previous sections the adjoint boundary condition can easily be modified to admit other figures of merit. The shape of the wing is constrained such that the maximum thickness to chord ratio remains constant between the initial and final designs. In addition, the mean angle of attack is allowed to vary to ensure the time-averaged coefficient of lift remains constant between designs.

The UFSYN107 developed by Nadarajah and Jameson, employs a non-linear frequency domain method in the solution of the unsteady Navier-Stokes equations. The NLFD adjoint based design procedures require the following steps:

1. **Periodic Flow Calculation at Constant Time Averaged Lift**. A set of multigrid cycles is used to drive the unsteady residual to a negligible value for all the modes used in the representation of the solution. In the case of a design process that constrains the time averaged lift, the mean angle of attack is perturbed every 10 multigrid cycles to maintain a constant time averaged coefficient of lift. This allows the unsteady residual to reduce by an order to two in magnitude before the angle is modified again.

2. **Adjoint Calculation**. The adjoint equation is solved by integrating in reverse time. With minor modifications, the NLFD numerical scheme employed to solve the flow equations is used to solve the adjoint equations in reverse time.

3. **Gradient Evaluation**. An integral over the last period of the adjoint solution is used to form the gradient. This gradient is then smoothed using an implicit smoothing technique. This ensures that each new shape in the optimization sequence remains smooth and acts as a preconditioner which allows the use of much larger steps. The smoothing leads to a large reduction in the number of design iterations needed for convergence. Refer to Nadarajah et al.[14] for a more comprehensive overview of the gradient smoothing technique. An assessment of alternative search methods for a model problem is given by Jameson and Vassberg.[9]

4. **Wing Shape Modification**. The wing shape is then modified in the direction of improvement using a steepest descent method.

   Let $\mathcal{F}$ represent the design variable, and $\mathcal{G}$ the gradient. An improvement can then be made with a shape change

   $$\delta\mathcal{F} = -\lambda\mathcal{G}.$$

5. **Grid Modification**. The internal grid is modified based on perturbations on the surface of the wing. The method modifies, the grid points along each grid index line projecting from the surface. The arc length between the surface point and the far-field point along the grid line is first computed, then the grid point at each location along the grid line is attenuated proportional to the ratio of its arc length distance from the surface point and the total arc length between the surface and the far-field.

6. **Repeat the Design Process**. The entire design process is repeated until the objective function converges. The problems in this work typically required between nine to twenty five design cycles to reach the optimum.

VI. Results

The following subsections presents results from simulations of a three-dimensional wing undergoing a change in angle of attack as a function of time.

$$\alpha(t) = \alpha_o + \alpha_m \sin(\omega t).$$

For the cases presented in this section, the mean angle of attack, α_o is $0.59°$ for the validation case and $0°$ for the design test cases. For both cases, the deflection angle, α_m is set to $\pm 0.25°$. The reduced frequency, $\frac{\omega c}{2V_\infty}$, is set to 0.102, with a far-field Mach number, M_∞, of 0.822. The wing is pitched about the 61.2% of the root chord. The flight conditions are based on *Run 73* of the central transonic test case CT5 conducted by R.J Zwaan at the NLR.[22]

The first part of the results section contains a code validation study. The study compares the convergence of the flow and adjoint solvers for various time steps per period, as well as, compare the lift hysteresis and drag and moment variation for various time steps per period. This is necessary to quantify the required number of time steps per period to establish a periodic steady state flow. The pressure distribution is compared to experimental data and prior inviscid results.[16] In the second section, a redesign of the LANN wing is demonstrated. Lastly, a gradient comparison between various number of temporal modes is presented and the convergence of the objective function.

A. Validation

The computational grid employed for the validation study is a structured grid as illustrated in Fig. 2. The MPI[13] domain topology is based on a $N_{p_i} = 4, N_{p_j} = 1, N_{p_k} = 3$, where N_p is the number of processors in each direction. In this work, four processors are used in the i direction, one in the j direction, and three in the k direction. Each processor contains a grid of size $n_x \times n_j \times n_k = 65 \times 65 \times 33$. The total grid is $257 \times 65 \times 97$. A cross-sectional view of the grid at the 20% and 65% span stations are shown in Fig. 3.

Figure 4 illustrates the convergence of the viscous NLFD flow solver. The convergence was obtained for the LANN Wing test case for three, five, and seven time steps per period. The zeroth mode for all cases converge at the same rate. The same is true for the first, second, and third modes. The flow solver residual attains a reduction of four orders of magnitude over 2400 multigrid cycles. For the design cases, only 200 cycles were employed per design cycle. Figure 5 (use Fig. 4 legend) illustrates the convergence of the viscous NLFD adjoint solver. Only 400 multigrid cycles were needed to converge the adjoint solver to the same level of accuracy as the flow solver. The rate of convergence is higher for the adjoint solver. All modes converge at similar rates.

The lift hysteresis is demonstrated in Fig. 6 for various number of time steps per period. Here, as indicated in the legend, 'NLFD 1-Harmonic' is synonymous to three time steps per period. As the wing oscillates at a small angle of attack, the shock wave moves back and forth about a mean location and is closely sinusoidal and lags the wing motion. This lag is evident in the lift hysteresis loop where the maximum lift does not occur at the maximum angle of attack. The nonlinear behavior of unsteady viscous transonic flows is primarily due to the movement of the shock and this is evident in Fig. 6. Figure 6 describes that one harmonic is sufficient to produce an accurate lift hysteresis. However, Fig. 7 demonstrates that at least two harmonics are needed to capture the variation of the drag coefficient versus angle of attack accurately. Figure 8 illustrates the variation in pitching moment and Fig. 9 demonstrates the variation of lift versus drag coefficient, further providing evidence that at least two harmonics are required to accurately capture the flow field for the LANN Wing, *Run 73*.

In Fig. 10, a validation of the surface pressure coefficient is presented. The figure illustrates the pressure distribution for two different angles of attacks at two separate span stations. In Fig. 10a results based on both the inviscid and viscous NLFD methods are compared to experimental data at the span location, $\eta = 20\%$ and angle of attack, $\alpha = 0.59°$. The inviscid NLFD results compare closely to the viscous solutions, however, the location of the shock for the inviscid NLFD solution differs by 5% of the chord. This is an expected result, since the location of the shock is generally dependent on viscous effects especially for unsteady flows. Apart from the shock location, the viscous NLFD solution resolves the peak pressure accurately. Nevertheless both solutions differ from the experimental work, and further research is necessary to investigate the discrepancy. One possible reason for the difference could be due to the effect of the turbulence model on the unsteady viscous flows. Figures 10b-d illustrate the comparison at the maximum angle of attack and at a different span location. Similar trends are observed for these conditions. The difference in the shock location and strength at the $\eta = 65\%$ span station is larger.

A second important outcome of Fig. 10 is the required number of time steps per period or modes to accurately resolve the pressure distribution. At the 20% span station, the 'NLFD 3 Viscous' case (indicating three time steps per period), is able to accurately produce the unsteady flow solution. However, at the 65% span location, a slight discrepancy is observed at the shock location. This is a further indication, that the viscous NLFD solutions require at least five time steps per period to resolve the flow field compared to the inviscid solution that only required three.

B. LANN wing: Redesign

This section documents the results of the redesign of the LANN Wing to reduce the time-averaged drag coefficient for a fixed time-averaged lift coefficient and wing thickness ratio. The simulation was performed at a Mach number, $M_\infty = 0.82$, reduced frequency, $\omega_r = 0.102$, and deflection of $\pm 0.25°$ about the zero angle of attack. As established in the previous section, five time steps per period were needed to accurately represent the variation of the drag coefficient versus angle of attack. Since the objective function is the time-averaged drag coefficient, five time steps will be used for the redesign of the LANN Wing. This decision will be further supported with a gradient accuracy study at the end of this section.

During the initial stage to compute the flow solution, the time-averaged lift and drag are computed and used as the target lift and objective function. During the subsequent design cycles, the mean angle of attack is modified at every ten multigrid cycles, to maintain the time-averaged lift coefficient. Ten multigrid cycles were chosen to allow the flow field to develop and to reduce the initial peak transient solutions admitted into the solution due to the change in angle of attack. At each design cycle, 200 multigrid cycles were used.

Figures 11-14 illustrate the wing surface pressure contour and the initial and final pressure distributions at three span locations at the 0°, 72°, 216°, and 288° phases after 50 design cycles. In Fig. 11, the pressure contour illustrates the severe weakening of the λ-shock system and this is further validated in the three pressure coefficient plots at span stations 6.2%, 49.2%, and 92.3%. The initial pressure distribution is illustrated as a dotted line, while the solid is at the final design. The plots, show a reduction of the shock wave strength at the mid-section with a decrease in the sectional drag coefficient from 0.0027 to 0.0014. The mean angle of attack was perturbed from the initial zero degrees to 0.344° to maintain the time-averaged lift coefficient at 0.348. The time-averaged drag coefficient reduced by 5.65% from 0.0115 to 0.01085 within 50 design cycles. The design is halted once the change in the objective function or time-averaged drag coefficient reaches a level of 1.E-6. The figure also demonstrates the initial and final, illustrated by a dotted and solid line, cross-sectional airfoil profiles. A distinctive feature of the new airfoil is the reduction of the upper surface curvature. The reduced curvature contributes to the weakening of the shock wave in the mid-section region of the LANN Wing. At the 72°, 216°, and 288° phases, as illustrated in Figs. 12 through 14, a severe weakening of the shock wave in the mid and tip sections of the LANN Wing are observed. At the 288° phase, a complete elimination of the shock wave is demonstrated.

Figures 15 and 16 demonstrate the initial and final three-dimensional surface pressure contour at the 0° and 288° phases. The weakening of the λ-shock is demonstrated in Fig. 15b. A complete elimination of the shock is observed at the 288° phase.

The Validation section illustrated the ability of the NLFD method to accurately model the flow with only five time steps per period. However, for the case of optimum shape design, the accuracy of the gradient of the objective function is of paramount importance. Figure 17 illustrate the gradients of the objective function at four different span locations for various temporal modes. The gradients are plotted in a clock-wise direction starting from the lower trailing edge to the leading edge and ending at the upper trailing edge point. The figures illustrate that with just three time steps per period, the gradients can be accurately captured at the 6% and 20% span stations, however, an additional mode or five time steps per period are required at the 65% and 91% stations. The gradients over a vast majority of the points at these stations agree very well, however, a large difference is observed between the 120 and 140 grid point. The points are adjacent to the shock location and as seen in the pressure distribution comparisons in Figs. 10c and d, an additional mode is required to resolve the gradient.

Lastly, Fig. 18 presents the convergence of the time-averaged drag coefficient from 115 drag counts to 108.5. Figure 19 shows the convergence of ΔI, where I is the objective function (time-averaged drag coefficient). ΔI reaches a level of 1.E-6 within 50 design cycles. During the first 35 design cycles, ΔI converges linearly as expected. Linear convergence is characteristic of a steepest descent type method. As the final wing profile is realized, the convergence increases rapidly. The code is automatically stopped as soon as a change of 1E-6 is detected. This level of change corresponds to a change to the sixth decimal place of the drag coefficient and this is sufficient for engineering accuracy.

VII. Conclusion

The NLFD method requires just five time steps per period to resolve the unsteady viscous transonic flow field. A redesign of the LANN Wing has been demonstrated with a reduction of the time-averaged drag coefficient by 5.65% while maintaning the time-averaged lift coefficient constant. The NLFD method with five time steps per period also provides accurate gradients. These results further demonstrate the potential of the method to provide significant improvements to more realistic problems such as helicopter rotors, turbomachinery, and other unsteady devices operating in the transonic regime.

References

[1] J. J. Adamczyk. Model equation for simulating flows in multistage turbomachinery. Technical report, NASA Technical Memorandum 86869., Nov 1984.

[2] R. Davis. Personal Communications on TFLO, January-December 2001.

[3] M. C. Duta, M. .B. Giles, and M. S. Campobasso. The harmonic adjoint approach to unsteady turbomachinery design. *International Journal for Numerical Methods in Fluids*, 40:323–332, October 2002.

[4] K. C. Hall. Seminar on harmonic balance techniques. Technical report, Presented to the Aerospace Computing Lab, Stanford University, 2000.

[5] K. C. Hall, J. P. Thomas, and W. S. Clark. Computation of unsteady nonlinear flows in cascades using a harmonic balance technique. Technical report, 9th International Symposium on Unsteady Aerodynamics, Aeroacoustics and Aeroelasticity of Turbomachines, Lyon, France, September 2000.

[6] A. Jameson. Computational aerodynamics for aircraft design. *Science*, 245:361–371, 1989.

[7] A. Jameson. Time dependent calculations using multigrid, with applications to unsteady flows past airfoils and wings. *AIAA paper 91-1596*, AIAA 10th Computational Fluid Dynamics Conference, Honolulu, Hawaii, June 1991.

[8] A. Jameson. Optimum aerodynamic design using CFD and control theory. *AIAA paper 95-1729*, AIAA 12th Computational Fluid Dynamics Conference, San Diego, CA, June 1995.

[9] A. Jameson and J. C. Vassberg. Studies of alternative numerical optimization methods applied to the brachistochrone problem. *OptiCON 99*, 1999.

[10] M. McMullen, A. Jameson, and J. Alonso. Acceleration of convergence to a periodic steady state in turbomachinery flows. *AIAA paper 01-0152*, 39th. Aerospace Sciences Meething and Exhibit, Reno, NV, Jan 2001.

[11] M. McMullen, A. Jameson, and J. Alonso. Application of a non-linear frequency domain solver to the euler and navier-stokes equations. *AIAA paper 02-0120*, 40th. Aerospace Sciences Meething and Exhibit, Reno, NV, Jan 2002.

[12] Matthew McMullen. *The Application of Non-Linear Frequency Domain Methods to the Euler and Navier-Stokes Equations.* Ph.d. dissertation, Department of Aeronautics and Astronautics, Stanford University, Stanford, CA, March 2003.

[13] Message Passing Interface Forum. *MPI: A Message-Passing Interface Standard*, May 1994. Available from http://www.mcs.anl.gov/Projects/mpi/index.html.

[14] S. Nadarajah and A. Jameson. Optimal control of unsteady flows using a time accurate method. *AIAA paper 2002-5436*, 9th. AIAA/ISSMO Symposium on Multidisciplinary Analysis and Optimization Conference, Atlanta, GA, September 2002.

[15] S. Nadarajah, A. Jameson, and J. J. Alonso. Sonic boom reduction using an adjoint method for wing-body configurations in supersonic flow. *AIAA paper 2002-5547*, 9th. AIAA/ISSMO Symposium on Multidisciplinary Analysis and Optimization Conference, Atlanta, GA, September 2002.

[16] S. Nadarajah, M. McMullen, and A. Jameson. Non-linear frequency domain based optimum shape design for unsteady three-dimensional flows. *AIAA paper 2006-1052*, 44th Aerospace Sciences Meeting and Exhibit, Reno, Nevada, January 2006.

[17] Siva Nadarajah. *The Discrete Adjoint Approach to Aerodynamic Shape Optimization.* Ph.d. dissertation, Department of Aeronautics and Astronautics, Stanford University, Stanford, CA, January 2003.

[18] J. Reuther, J.J. Alonso, M.J. Rimlinger, and A. Jameson. Aerodynamic shape optimization of supersonic aircraft configurations via an adjoint formulation on parallel computers. *AIAA paper 96-4045*, 6th AIAA/NASA/ISSMO Symposium on Multidisciplinary Analysis and Optimization, Bellevue, WA, September 1996.

[19] J. Reuther, A. Jameson, J. Farmer, L. Martinelli, and D. Saunders. Aerodynamic shape optimization of complex aircraft configurations via an adjoint formulation. *AIAA paper 96-0094*, 34th Aerospace Sciences Meeting and Exhibit, Reno, Nevada, January 1996.

[20] A. Snider. An Improved Estimate of the Accuracy of Trigonometric Interpolation. *SIAM Journal on Numerical Analysis*, 9(3):505–508, 1972.

[21] J. P. Thomas, K. C. Hall, and E. H. Dowell. A discrete adjoint approach for modelling unsteady aerodynamic design sensitivities. *AIAA paper 03-0041*, 41th. Aerospace Sciences Meething and Exhibit, Reno, NV, Jan 2003.

[22] R. J. Zwaan. Data set 9, LANN wing. Pitching oscillation. Technical report. Agard-R-702 Addendum no. 1., AGARD, Amsterdam, Netherlands, 1985.

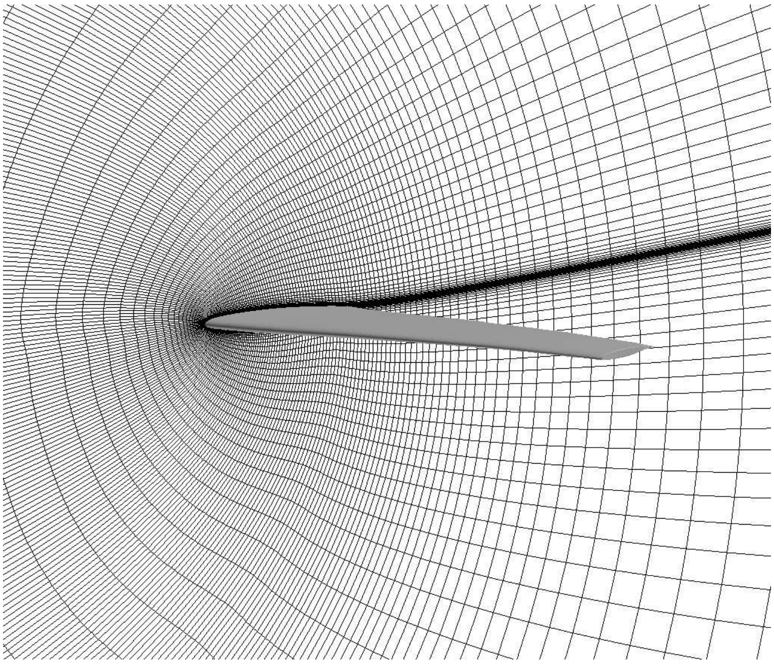

(a) LANN Wing Mesh

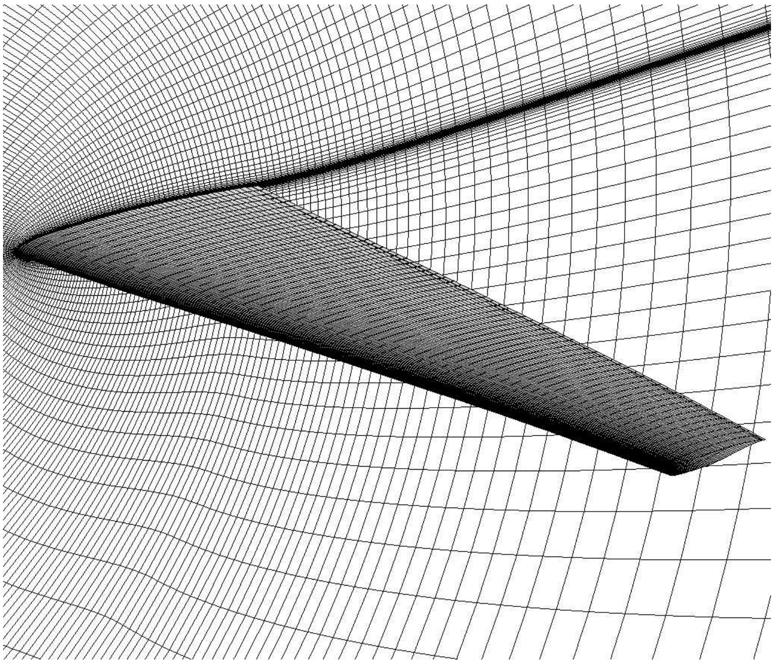

(b) Close-up View

Figure 2. LANN Wing Grid Structure; MPI Domain Topology, $N_{p_i} = 4, N_{p_j} = 1, N_{p_k} = 3$**; Grid Size** $n_x \times n_j \times n_k = 257 \times 65 \times 97$

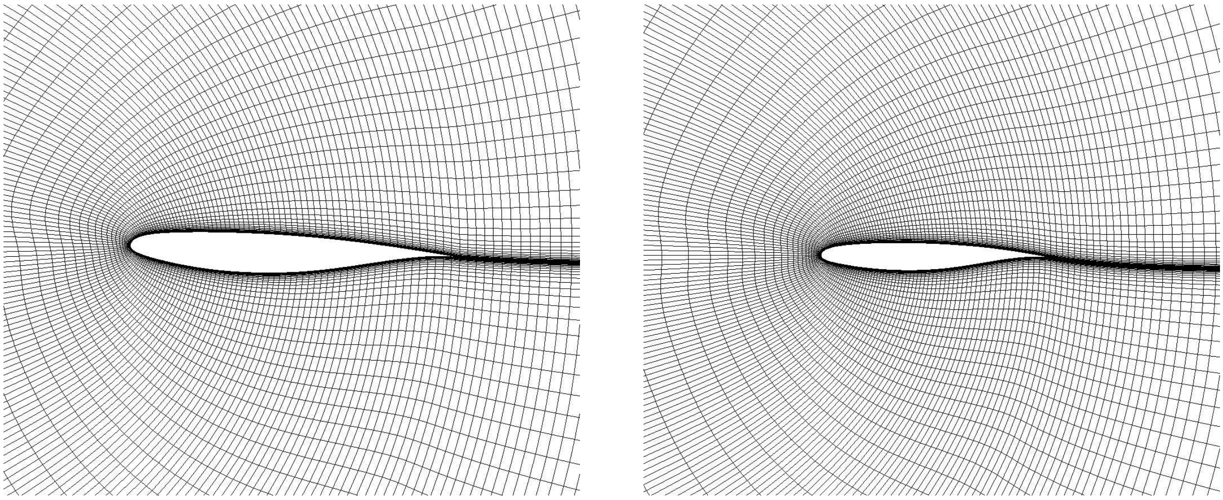

(a) Mesh Cross-Section at 20% span

(b) Mesh Cross-Section at 65% span

Figure 3. LANN Wing Mesh; Grid Size $n_x \times n_j \times n_k = 257 \times 65 \times 97$

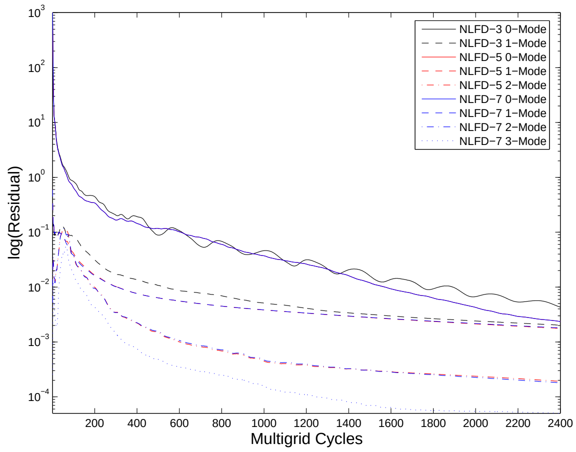

Figure 4. Viscous NLFD Flow Solver Convergence; $M_\infty = 0.822$, $\omega_r = 0.102$

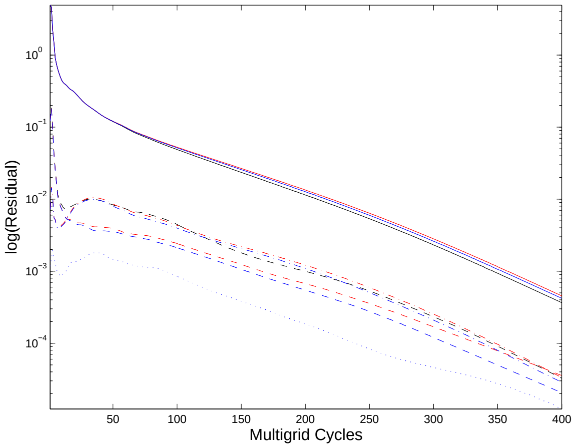

Figure 5. Viscous NLFD Adjoint Solver Convergence; $M_\infty = 0.822$, $\omega_r = 0.102$

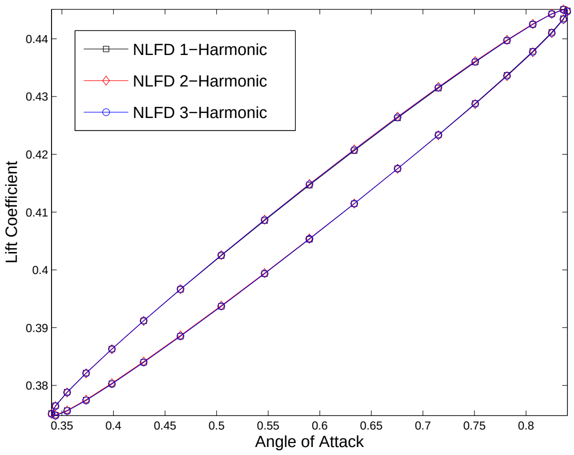

Figure 6. Comparison of Lift Hysteresis for Various Modes, LANN Wing: Run 73, $M_\infty = 0.82$, $\omega_r = 0.102$

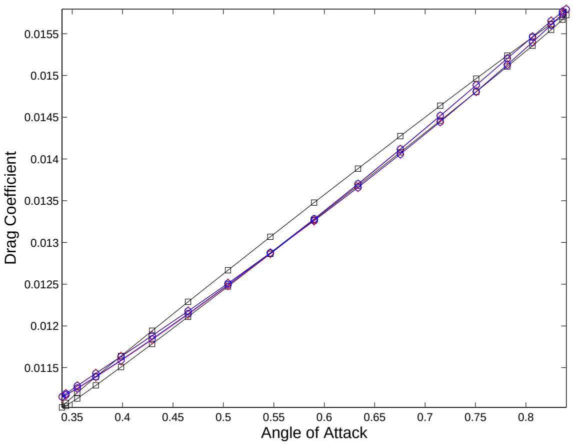

Figure 7. Comparison of Variation of Drag Coefficient versus Angle of Attack for Various Modes, LANN Wing: Run 73, $M_\infty = 0.82$, $\omega_r = 0.102$

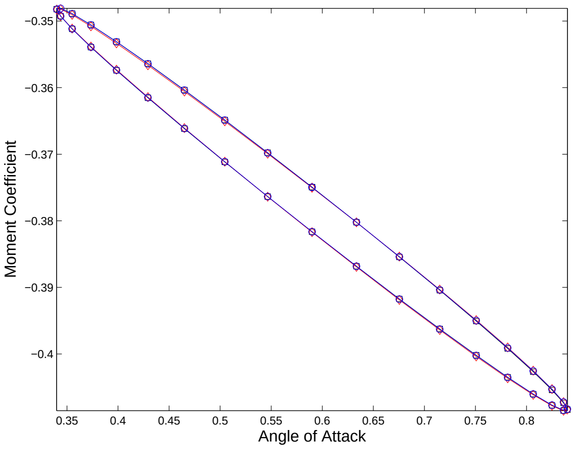

Figure 8. Comparison of Variation of Pitching Moment Coefficient versus Angle of Attack for Various Modes, LANN Wing: Run 73, $M_\infty = 0.82$, $\omega_r = 0.102$

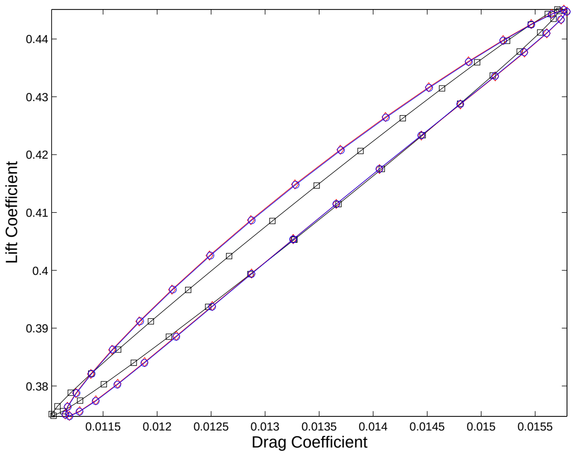

Figure 9. Comparison of Lift versus Drag Coefficient for Various Modes, LANN Wing: Run 73, $M_\infty = 0.82$, $\omega_r = 0.102$

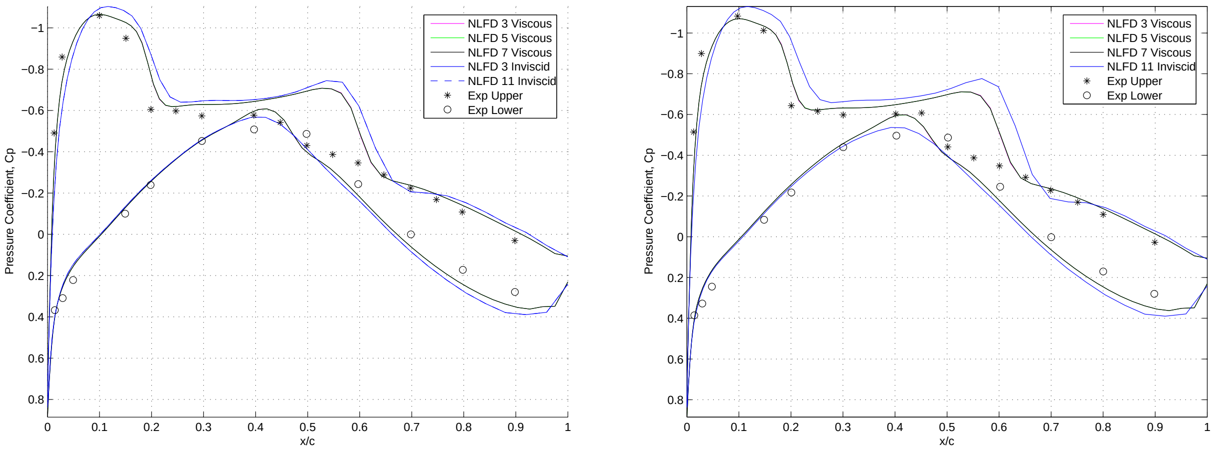

(a) $\eta = 20\%, \alpha = \alpha_{mean} = 0.59°$ (b) $\eta = 20\%, \alpha = \alpha_{max} = 0.84°$

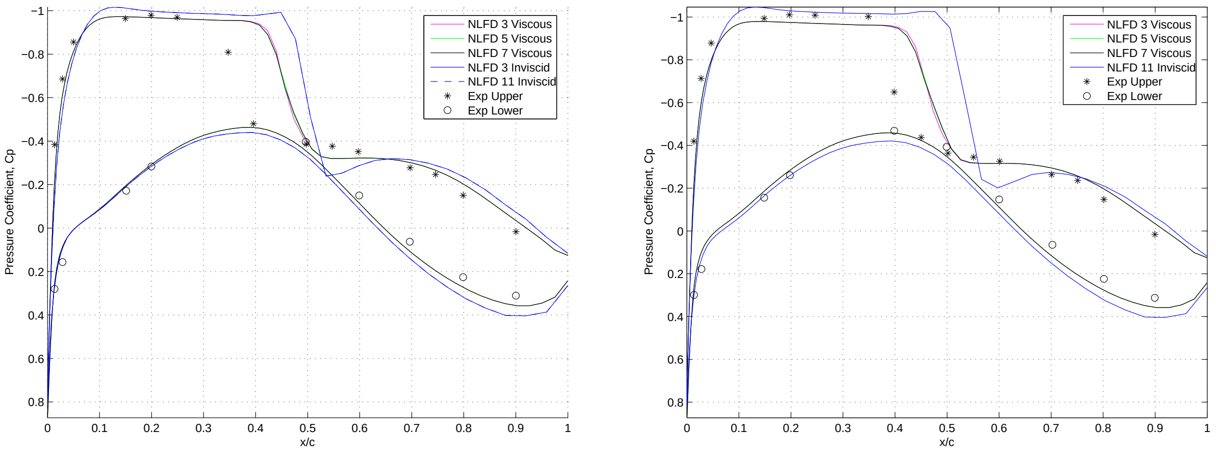

(c) $\eta = 65\%, \alpha = \alpha_{mean} = 0.59°$ (d) $\eta = 65\%, \alpha = \alpha_{max} = 0.84°$

Figure 10. Comparison of Pressure Distribution between Inviscid, Viscous, and Experimental Data for LANN Wing, Run 73, $M_\infty = 0.82$, $\omega_r = 0.102$

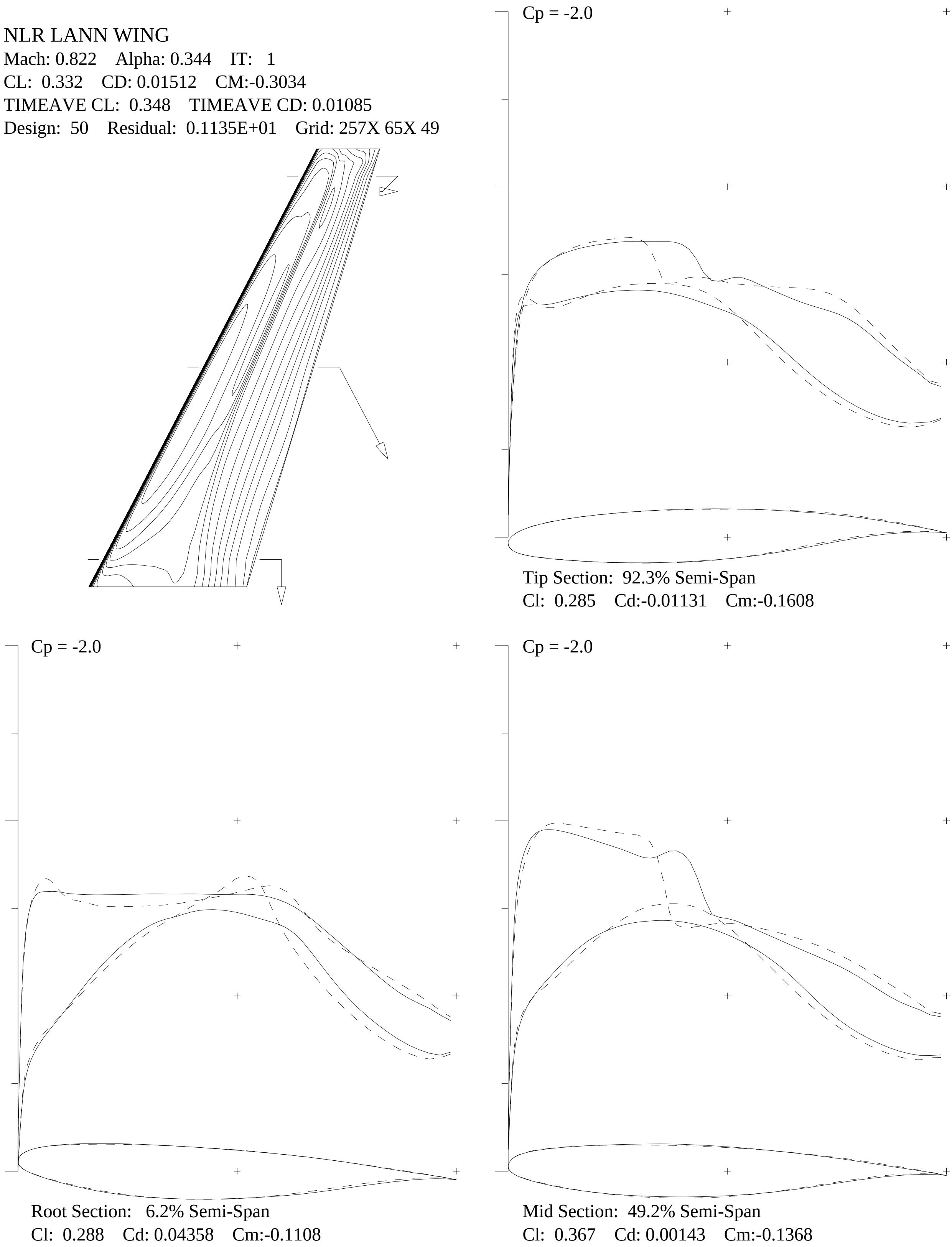

Figure 11. Initial and Final Pressure Distribution for Various Span Locations at Phase = 0 deg

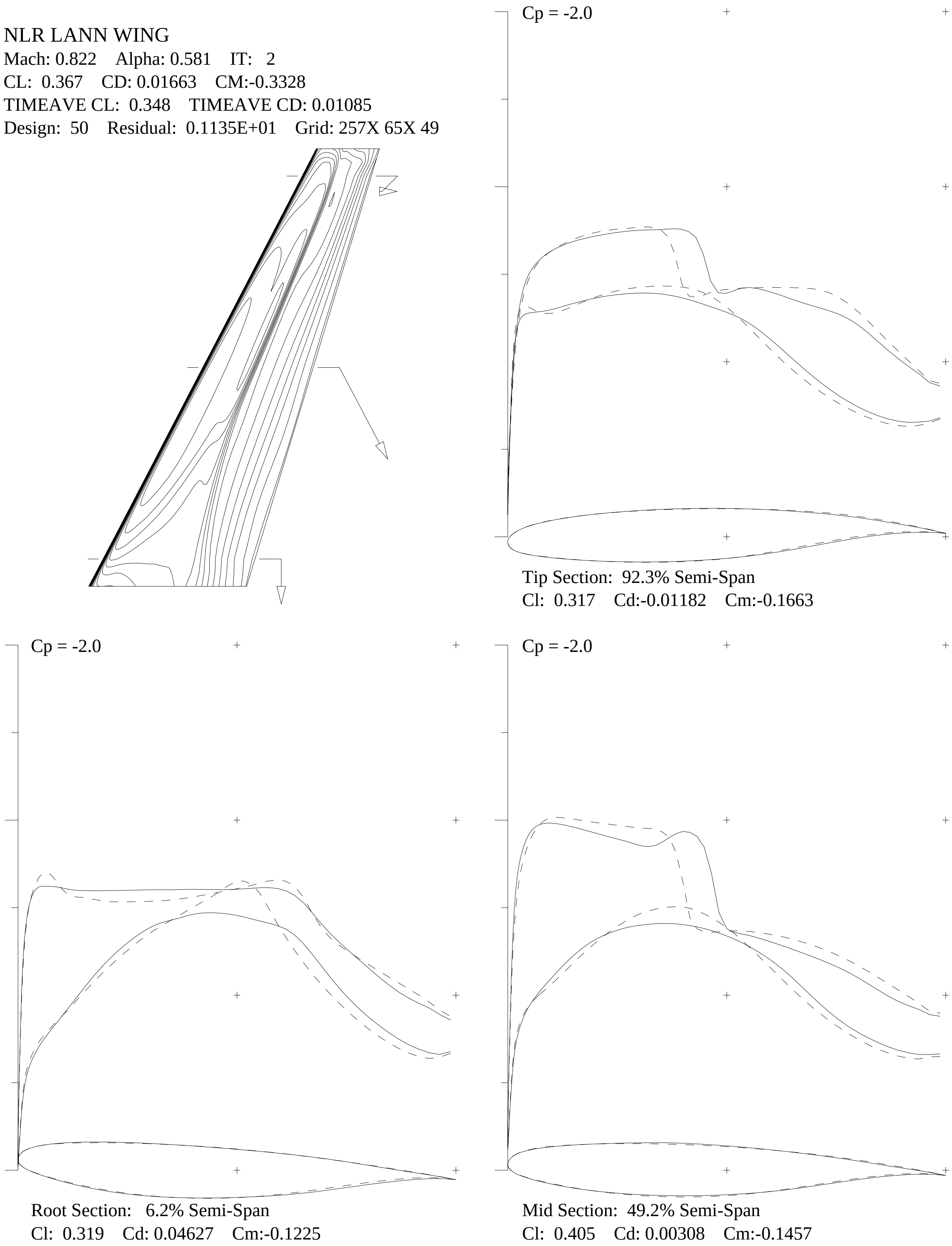

Figure 12. Initial and Final Pressure Distribution for Various Span Locations at Phase = 72 deg

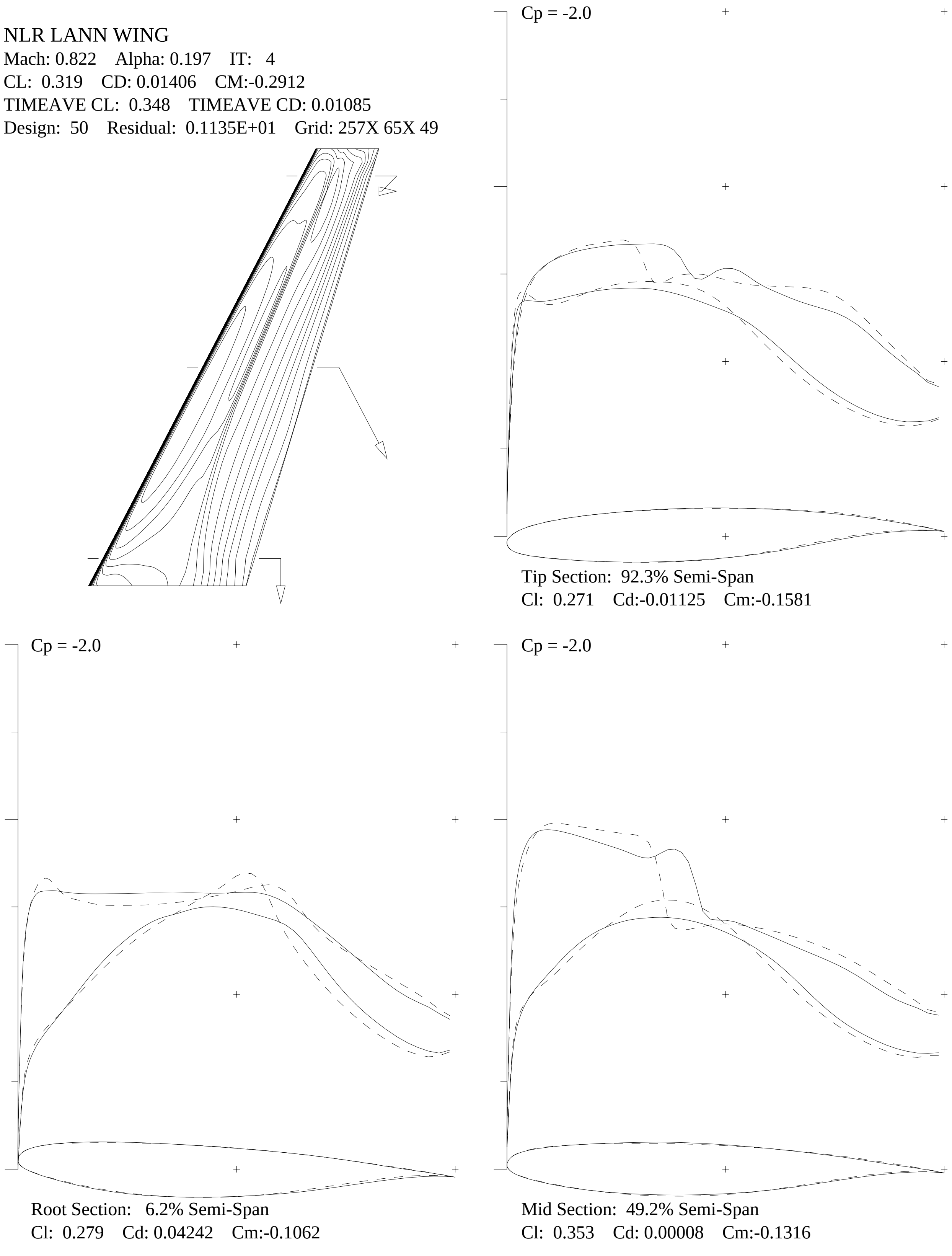

Figure 13. Initial and Final Pressure Distribution for Various Span Locations at Phase = 216 deg

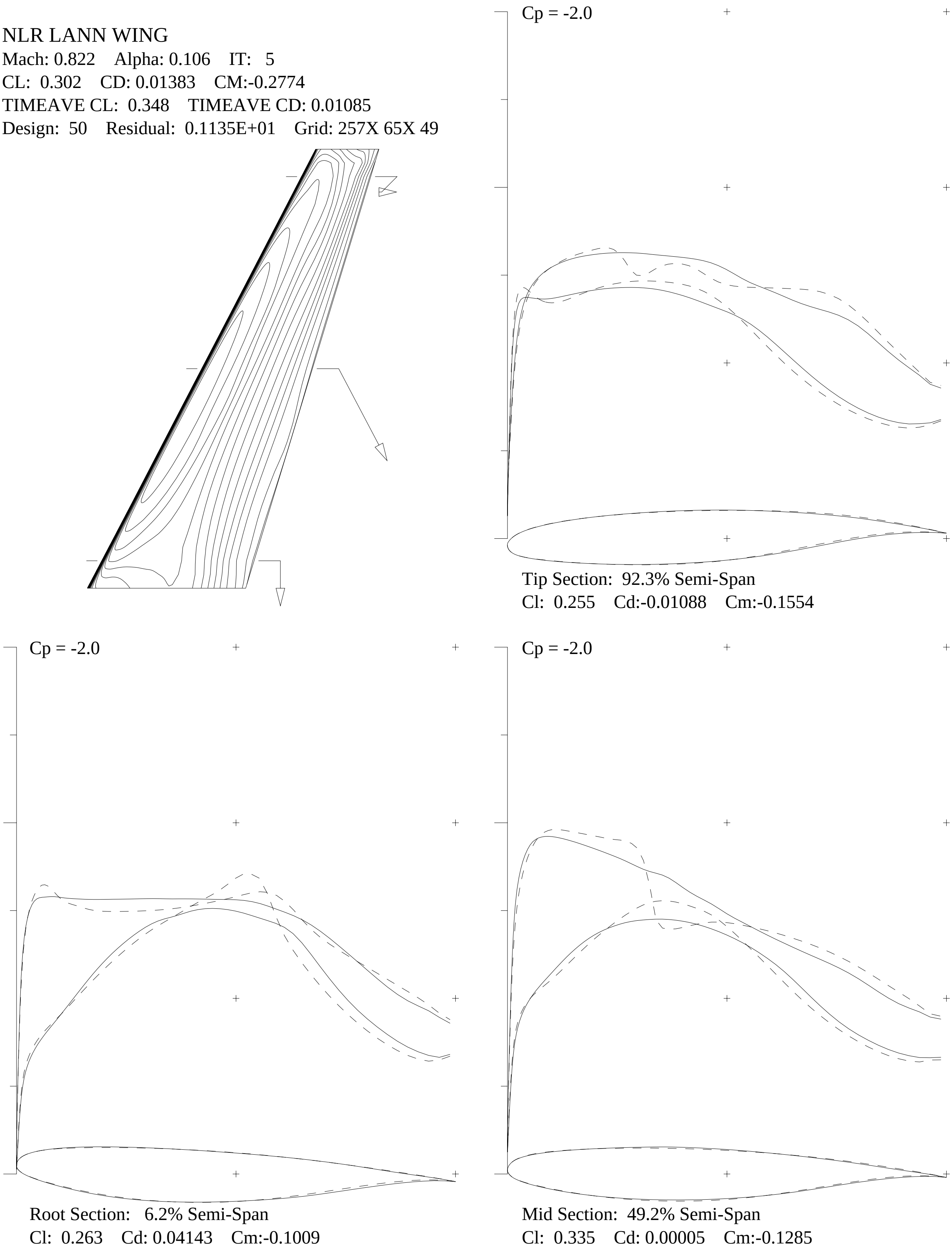

Figure 14. Initial and Final Pressure Distribution for Various Span Locations at Phase = 288 deg

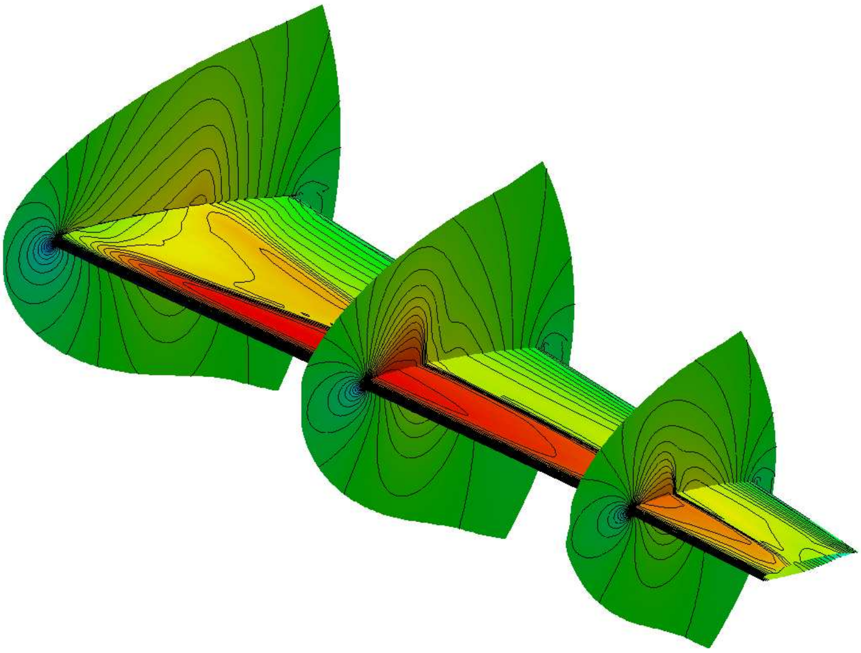

(a) Initial Surface Pressure Contour

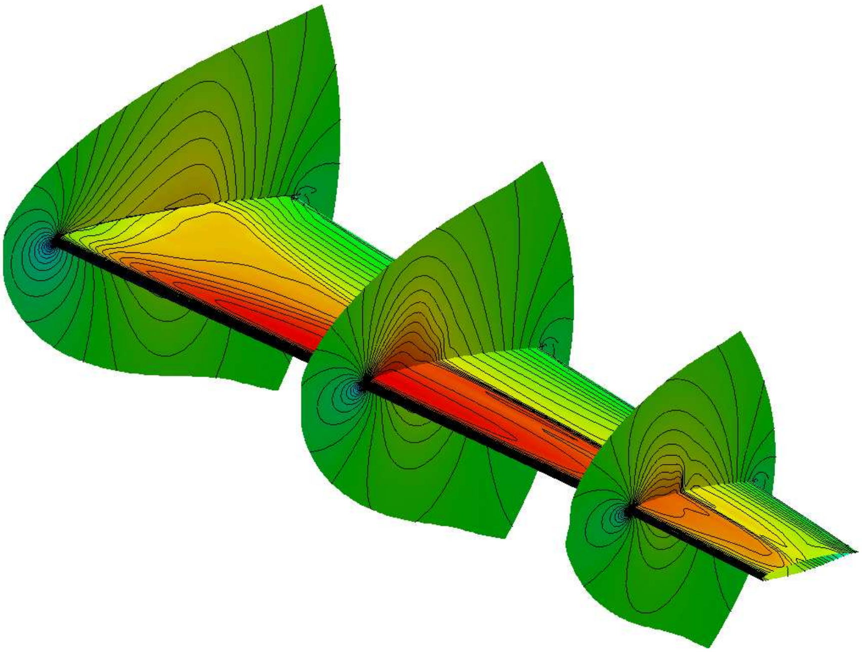

(b) Final Surface Pressure Contour

Figure 15. Initial and Final Surface Pressure Contours at 0° **Phase for the LANN Wing, Run 73,** $M_\infty = 0.82$, $\omega_r = 0.102$

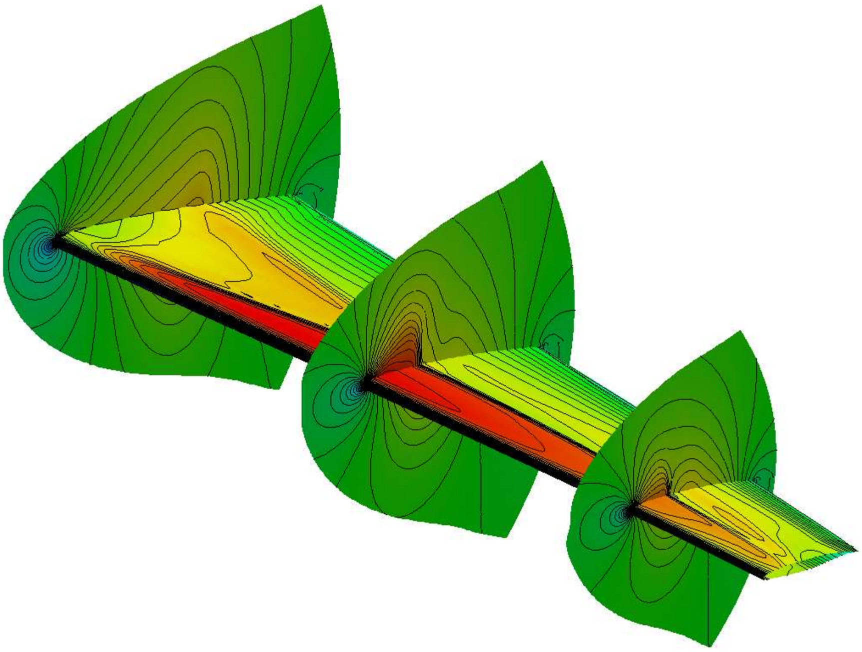

(a) Initial Surface Pressure Contour

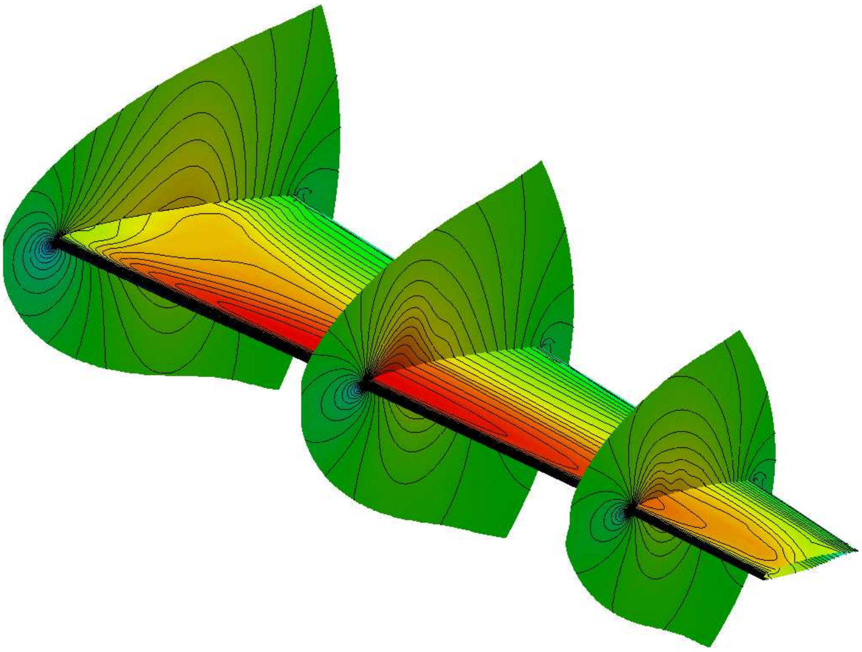

(b) Final Surface Pressure Contour

Figure 16. Initial and Final Surface Pressure Contours at $288°$ **Phase for the LANN Wing, Run 73,** $M_\infty = 0.82$, $\omega_r = 0.102$

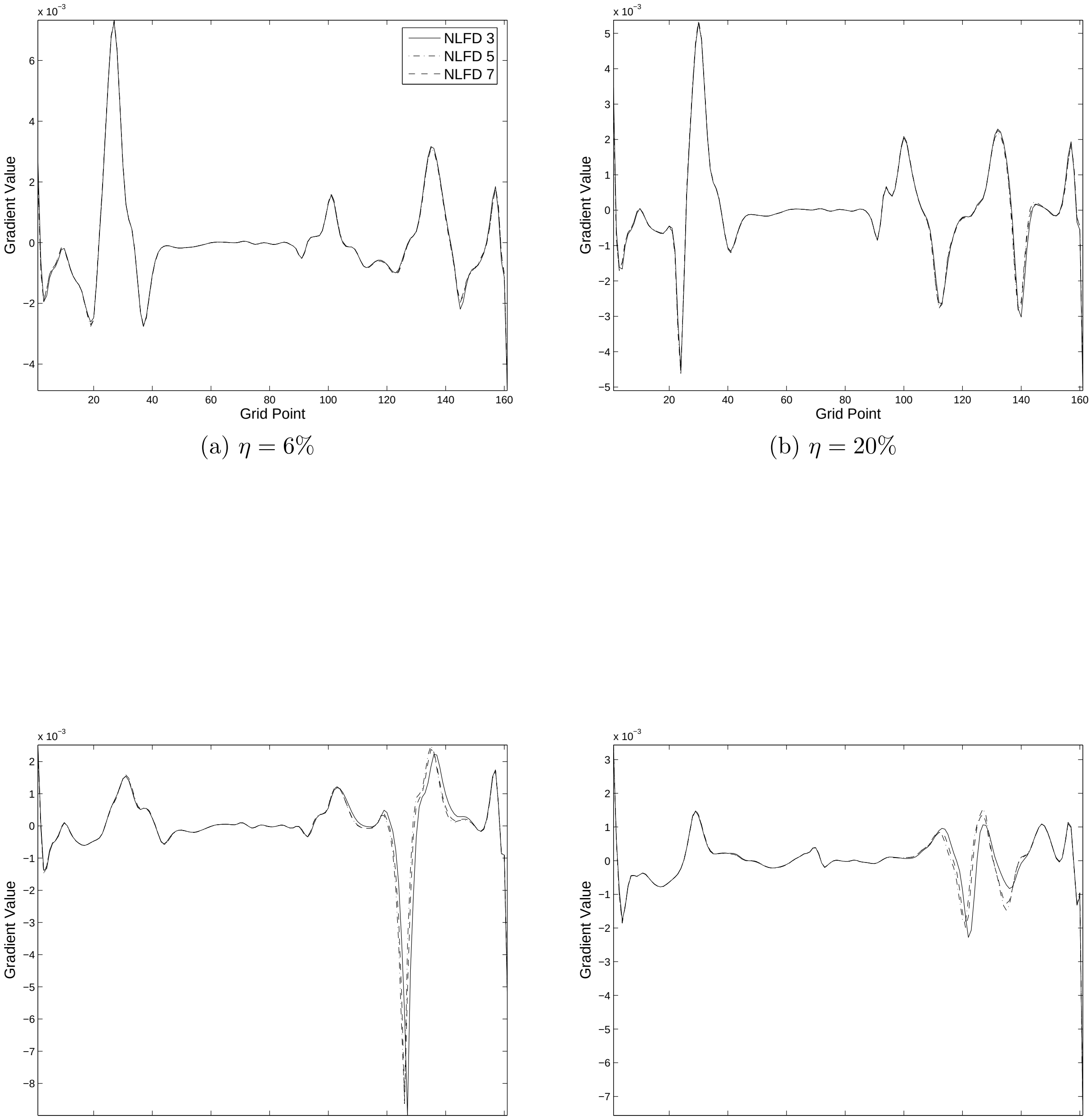

(a) $\eta = 6\%$

(b) $\eta = 20\%$

(c) $\eta = 65\%$

(d) $\eta = 91\%$

Figure 17. Comparison of Gradient for Various Modes for the LANN Wing, Run 73, $M_\infty = 0.82$, $\omega_r = 0.102$

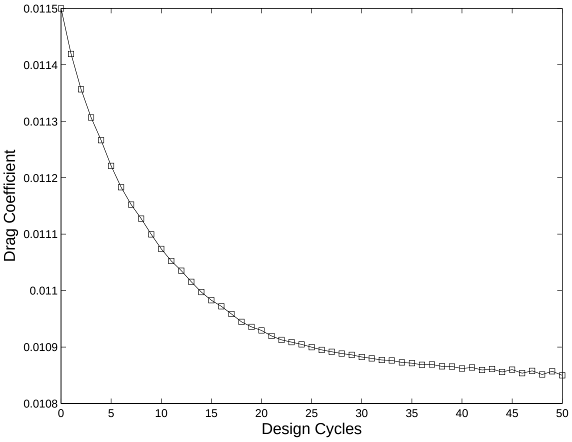

Figure 18. Convergence of Time-Averaged Drag Coefficient

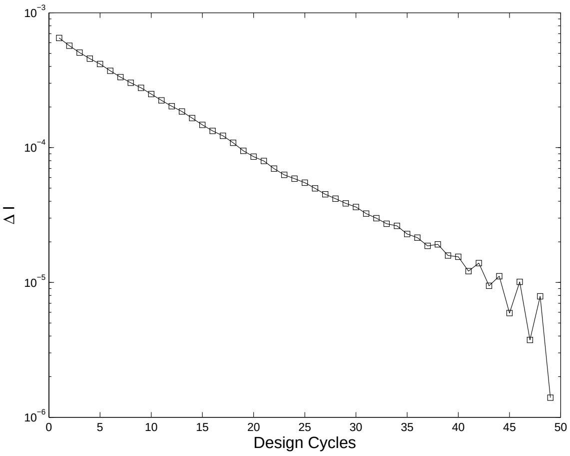

Figure 19. Convergence of the Change in the Objective Function, ΔI